ChemComm

Check for updates

Fluorinated cryptophane-A and porphyrin-based theranostics for multimodal imaging-guided photodynamic therapy†

Huaibin Zhang,[ab] Qiao Yu,[a] Yu Li,[b] Zhigang Yang, [ID][a] Xin Zhou, [ID][b] Shizhen Chen*[b] and Zhong-Xing Jiang [ID]*[a]

Herein, we developed fluorinated nanoemulsions with significantly enhanced *in vitro* and *in vivo* [129]Xe hyper-CEST MRI, ^{19}F MRI and fluorescence imaging signals for selective and sensitive tumor detection and NIR-activated photodynamic therapy.

Although oncology has gained tremendous advances in recent years, the development of novel strategies for cancer accurate diagnosis and effective therapy remains a major task. On the diagnosis side, selective and sensitive detection of cancer cells is crucial for early diagnosis, effective intervention, and high survival rate, which requires the exquisite application of modern molecular biology and imaging technology. As one of the most used imaging technologies in oncology, proton magnetic resonance imaging (^{1}H MRI) suffers huge background signals and low sensitivity, which limits its ability to detect low-abundance biomarkers of cancer. To this end, ^{19}F MRI[1] and [129]Xe hyper-CEST MRI[2] are attractive complimentary technologies. The lack of ^{19}F and [129]Xe signals in biological systems facilitates ^{19}F MRI and [129]Xe hyper-CEST MRI with highly selective "hot-spot" images of targets without background interference.[1,2] In terms of sensitivity, the hyper-CEST technology of [129]Xe MRI can increase the sensitivity by over 1 000 000-fold, which facilitates the sensitive detection of biomarkers at a pM level.[2] It is noteworthy that both ^{19}F and [129]Xe are stable natural isotopes. [19]F MRI is an "always on" tracer technology for ^{19}F-labeled targets, such as drugs, nanoparticles, cells, biomolecules, *etc.*[1] While, [129]Xe hyper-CEST MRI is a versatile

"on-call" tracer technology without prior [129]Xe labelling of the targets, which alleviates the difficulties in labelling low-abundance biomarkers.[2] So, it would be highly beneficial to integrate the two complimentary technologies into a diagnosis or tracer system.[3] On the therapy side, the most widely used chemotherapy suffers many drawbacks, such as toxic side effects, drug resistance, and the need for other forms of treatment. As a compliment to chemotherapy, photodynamic therapy (PDT) ablates cancer cells with a photosensitizer and light of a specific wavelength in a noninvasive and low toxic way without multi-drug resistance.[4] In addition, high therapeutic efficacy can be achieved by the integration of multimodal imaging and therapeutic agents into theranostics which take the advantages of comprehensive multi-dimensional drug-tumor-therapy information from each imaging technology for accurate cancer diagnosis and personalized therapy.[5] Therefore, it would be of great interest to incorporate ^{19}F MRI, [129]Xe hyper-CEST MRI, and PDT into novel theranostics.

To develop such theranostics, "add-on" strategy-based fluorinated nanoemulsions **Eml-RGD** were herein designed (Fig. 1), which contained fluorinated dendron **1** in the core and fluorinated cryptophane-A **2** and tetrabenzylporphyrin **3** on the surface. Cryptophane-A and tetrabenzylporphyrin are highly hydrophobic and severely aggregate in water, which leads to imaging signal quenching and low PDT efficacy. Here, they were modified into fluorinated amphiphilic "add-on" modules **2** and **3** with monodisperse polyethylene glycols (M-PEGs) as solubility and biocompatibility enhancers.[6] After being self-assembled onto the lipoid surfaces through hydrophobic and fluorous interactions, **2** would capture exchangeable hyperpolarized [129]Xe in the system and generate [129]Xe hyper-CEST MRI, while **3** would generate fluorescence imaging (FL) and reactive oxygen species (ROS) for PDT. To avoid ^{19}F MRI chemical shift artifacts and improve ^{19}F MRI sensitivity and hydrophobic interactions, a dendron with 27 symmetrical fluorines was integrated into **1**, **2** and **3**, respectively, which were supposed to give a united ^{19}F signal for highly sensitive ^{19}F MRI. In turn, the high O_2 solubility in fluorinated nanoemulsions would facilitate the delivery of O_2 to

[a] Hubei Province Engineering and Technology Research Center for Fluorinated Pharmaceuticals and School of Pharmaceutical Sciences, Wuhan University, Wuhan 430071, China. E-mail: zxjiang@whu.edu.cn

[b] State Key Laboratory of Magnetic Resonance and Atomic and Molecular Physics, National Center for Magnetic Resonance in Wuhan, Wuhan Institute of Physics and Mathematics, Innovative Academy of Precision Measurement Science and Technology, Chinese Academy of Sciences, Wuhan, 430071, China. E-mail: chenshizhen@wipm.ac.cn

Communication

Fig. 1 Structure of multifunctional theranostics **Eml-RGD**.

Fig. 2 DLS and TEM (a, scale bar = 100 nm), UV absorption (b), fluorescence emission (c), ^{19}F NMR (d, 471 MHz, chemical shift (ppm) for **1**: −72.2, **2**: −71.4, **3**, −71.8, **Eml**: −72.2, **Eml-RGD**: −72.2, TFE (internal standard): −76.7, D$_2$O as solvent for **2** and **3**), ^{19}F MRI (e, 9.4T) and SI *versus* C(^{19}F) plot (f), and concentration-dependent ^{129}Xe hyper-CEST NMR (g) of the nano-emulsions.

hypoxic tumors and promote the *in vivo* PDT efficacy. Cholesterol-labeled targeting peptide Cls-PEG-RGDyC was incorporated into the nanoparticles to achieve selective imaging and targeted PDT of cancer cells with a high expression of integrin $\alpha_v\beta_3$.[3]

The components of **Eml-RGD** were then synthesized (ESI†). Dendron **1** was conveniently synthesized in 1 step on a 32.5 gram scale. With the key intermediates **17** and **21**, "add-on" modules **2** and **3** were efficiently synthesized in convergent ways. Cls-PEG-RGDyC **24** was prepared by conjugating commercially available RGDyC **22** and cholesterol-PEG$_{2000}$-maleimide **23** in PBS. With these fully characterized components, fluorinated nanoemulsions **Eml-RGD** as well as nanoemulsions **Eml** without Cls-PEG-RGDyC, were then formulated with lipoid S75 and F68 as the emulsifiers (ESI†). Dynamic light scattering (DLS) showed particle sizes of 130 nm (polydispersity index, PDI = 0.18) and 125 nm (PDI = 0.15) for **Eml-RGD** and **Eml**, respectively, which were further confirmed by transmission electron microscopy (TEM, Fig. 2a). As tetrabenzylporphyrin is an ideal fluorophore, the nanoemulsions showed distinctive UV absorption peaks at 420 nm, 515 nm, 553 nm, 590 nm, and 650 nm (Fig. 2b), and fluorescence emission peaks at 658 nm and 724 nm (Fig. 2c). As expected, **1**, **2**, **3**, **Eml-RGD** and **Eml** all gave a singlet ^{19}F NMR peak, respectively (Fig. 2d). Although there were ^{19}F chemical shift differences among pure components **1–3**, no ^{19}F signal splitting was observed in **Eml-RGD** and **Eml**, which indicated that add-on modules **2** and **3** indeed self-assembled onto the surface of the nanoparticles and all the ^{19}F were under similar environments. ^{19}F MRI phantom images showed the high sensitivity of **Eml-RGD** and **Eml**, which were detected at a low ^{19}F concentration of 16.9 mM with a short scan time of 160 seconds (or 1.78×10^{17} spin per voxel, Fig. 2e). Notably, their ^{19}F MRI signal intensities (SI) were proportional to their ^{19}F concentrations, which facilitates local ^{19}F concentration quantification with ^{19}F MRI SI (Fig. 2f). When **Eml-RGD** was exposed to hyperpolarized ^{129}Xe gas, a concentration-dependent ^{129}Xe hyper-CEST NMR signal from cryptophane-A captured ^{129}Xe at 72 ppm was detected (Fig. 2g and Fig. S3, ESI†). High stability of **Eml-RGD** and **Eml** over a month was found by DLS monitoring of the particle sizes (Fig. S2, ESI†).
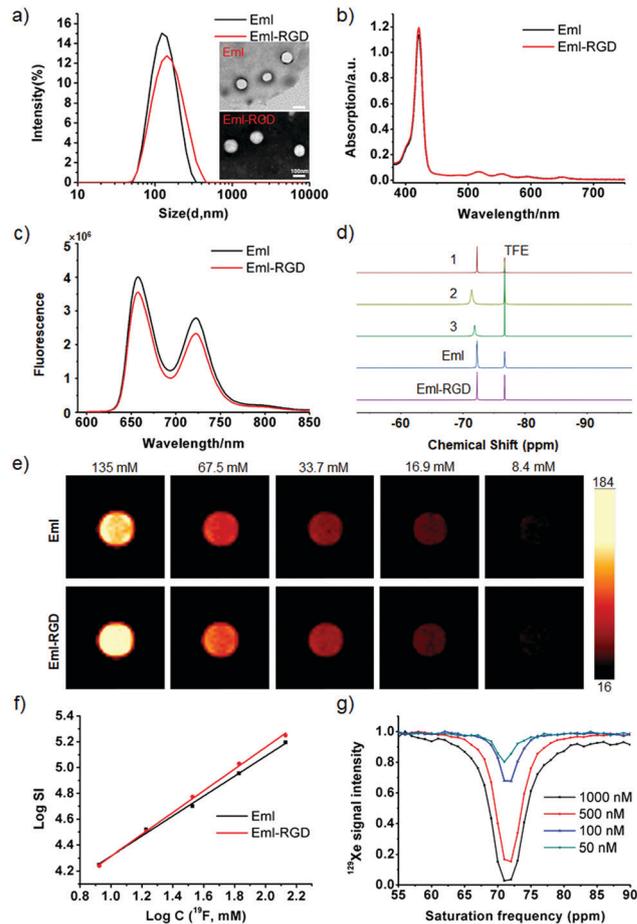
Selective multimodal imaging detection of integrin $\alpha_v\beta_3$ over expressed cancer cells with **Eml** and **Eml-RGD** was carried out on human lung cancer A549 cells (high $\alpha_v\beta_3$ expression) and human breast cancer MCF-7 cells (low $\alpha_v\beta_3$ expression). **Eml** and **Eml-RGD** exhibited high biocompatibility in A549 cells and MCF-7 cells (Fig. S4, ESI†). From the confocal microscopy images of **Eml** and **Eml-RGD** treated A549 cells and MCF-7 cells, the highest fluorescence intensity from **3** was detected in **Eml-RGD** treated A549 cells, which was up to 240% higher than the others (Fig. 3a). Interestingly, the highest SI in **Eml-RGD** treated A549 cells was also detected by ^{19}F MRI and ^{129}Xe hyper-CEST MRI (Fig. 3c and e). Notably, quantitative comparison of the three imaging technologies by plotting of the relative SI in the nanoemulsion treated cells showed a highly consistent trend (Fig. 3b, d and f). Therefore, nanoemulsions **Eml-RGD** provided three imaging technologies for quantitative and selective detection of integrin $\alpha_v\beta_3$ over expressed cancer cells.

The cytotoxicity and PDT efficacy of **Eml-RGD** were investigated in A549 cells. First, **Eml-RGD** exhibited little cytotoxicity towards A549 cells, while, after 5 min of 650 nm laser irradiation
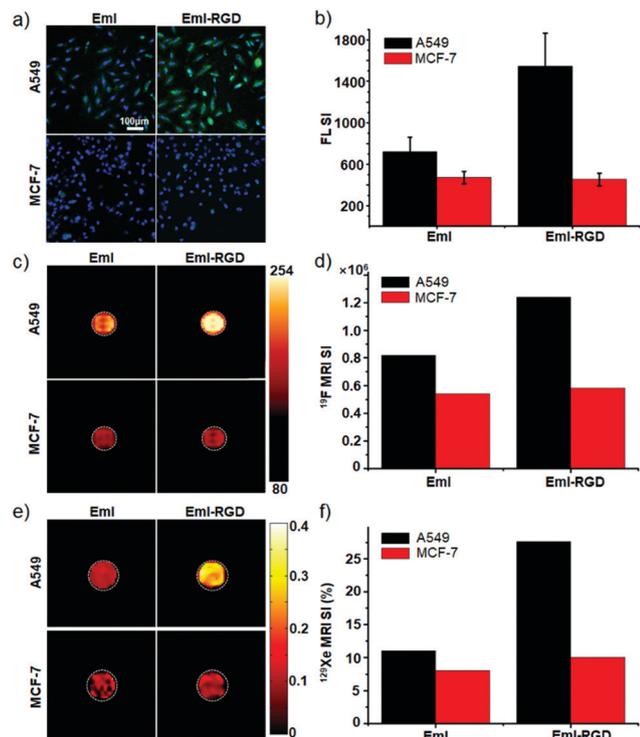
Fig. 3 Confocal images (a, blue: DAPI; green: **3**) and SI plot (b), ^{19}F MRI (c) and SI plot (d), ^{129}Xe hyper CEST MRI (e) and SI plot (f) of **Eml** and **Eml-RGD** treated A549 cells and MCF-7 cells.
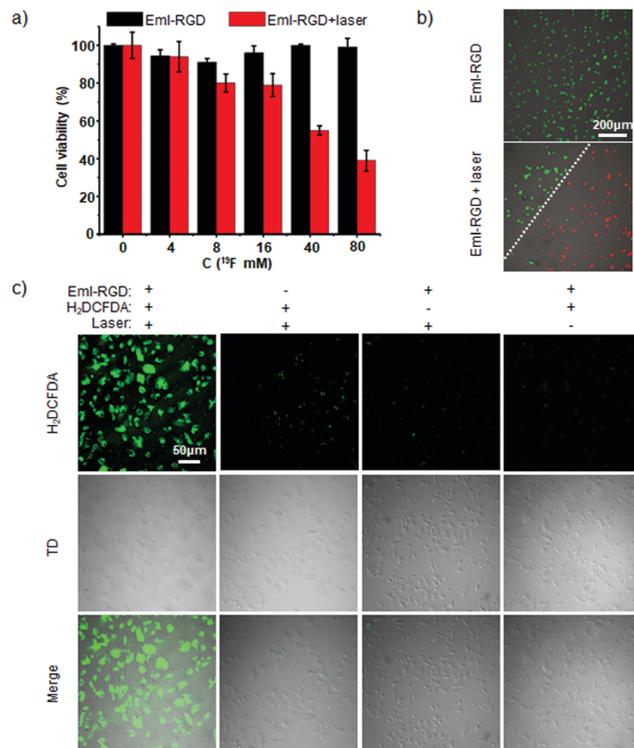

Fig. 4 Cytotoxicity assay (a), fluorescence images of live/dead cell staining (b), and confocal images of A549 cells in the presence or absence of laser irradiation (c), **Eml-RGD** treatment and H$_2$DCFDA.
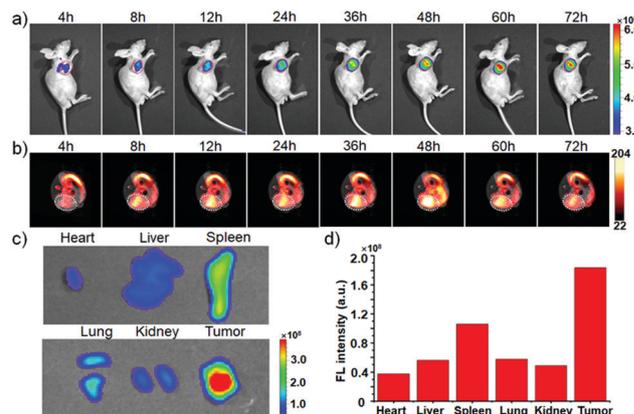
at 100 mW cm^{-2}, high cytotoxicity was found in **Eml-RGD** treated A549 cells (C(^{19}F) = 80 mM, Fig. 4a). Second, with the green fluorescence from calcein-AM stained live cells and red fluorescence from PI stained dead or later apoptosis cells, a clear border between live and dead cells around the light spot was observed from **Eml-RGD** treated A549 cells after 10 min of 650 nm laser irradiation at 100 mW cm^{-2}, which indicated the high PDT efficacy of **Eml-RGD** (Fig. 4b). Finally, using a reactive oxygen species (ROS) probe H$_2$DCFDA which emits green fluorescence in the presence of ROS, the ability of **Eml-RGD** to generate ROS under laser irradiation was evaluated. Without **Eml-RGD** treatment or 650 nm laser irradiation, neglectable ROS in A549 cells was detected by the green fluorescence of H$_2$DCFDA (Fig. 4c, column 2 & 4), while strong green fluorescence was detected from **Eml-RGD** and 650 nm laser treated A549 cells (Fig. 4c, column 1). Therefore, **Eml-RGD** can significantly improve the oxidative stress of A549 cells and effectively kill the cells after a low power density 650 nm laser irradiation.

On a xenograft A549 tumor nude mouse model, *in vivo* dual-imaging with **Eml-RGD** was carried out. After intravenous injection of **Eml-RGD**, and the FL showed the accumulation of **Eml-RGD** in the tumor with high convenience and sensitivity (dose = 27 mM kg^{-1} of ^{19}F, Fig. 5a). Meanwhile, the "hot-spot" ^{19}F MRI showed more detailed accumulation of **Eml-RGD** in deep organs and the tumor with a scan time of 17 min (dose = 27 mM kg^{-1} of ^{19}F, Fig. 5b). A peak **Eml-RGD** intensity in the tumor at 48 h post injection was found by *in vivo* ^{19}F MRI. Furthermore, the accumulation of **Eml-RGD** in the tumor and

Fig. 5 *In vivo* FL (a), ^{19}F MRI (b, a tumor-containing cross section) of mice after intravenous injection of Eml-RGD, *ex vivo* FL (c) and quantitative FL analysis (d) of organs and the tumor at 72 h ($n = 3$).

organs was quantitatively analyzed with the *ex vivo* FL (Fig. 5c), which indicated the high tumor accumulation of **Eml-RGD** (Fig. 5c and d). As a pair of complimentary imaging technologies, FL facilitated the quantitative detection of **Eml-RGD** in superficial tumors and *ex vivo* tissues in a convenient and sensitive way, while ^{19}F MRI provided detailed information about the distribution and concentration of **Eml-RGD** in deep tissues in a non-invasive and quantitative way. With the targeting effect of RGDyC and enhanced permeability and retention (EPR)
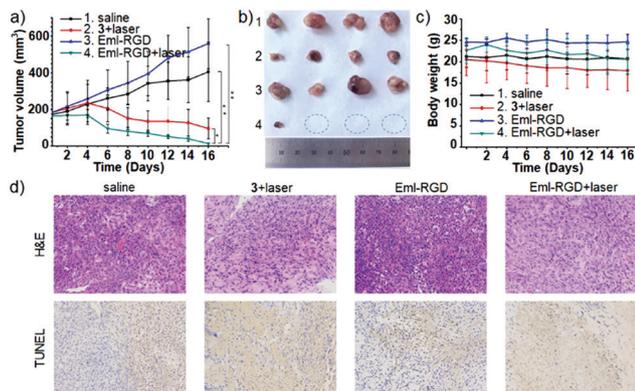
Fig. 6 Tumor growth graph (a, $p < 0.05$ (*), $p < 0.0001$ (**)), tumor photos (b, collected on day 16), and body weight graph (c) of mice after group treatments, tumor H&E and TUNEL staining (d, tumor collected on day 16). Graphs a and c were expressed as mean $\pm$ SD, $n = 4$.

effect of nanoemulsions, the high tumor accumulation of **Eml-RGD** was confirmed by dual-modal *in vivo* and *ex vivo* imaging.

Finally, *in vivo* cancer PDT was investigated in 4 groups of xenograft A549 tumor mice. When the tumor sizes reached 170 mm^3, the mice in group 1–4 were intravenously dosed with saline, tetrabenzylporphyrin 3, **Eml-RGD**, and **Eml-RGD** plus 15 min of 650 nm laser irradiation at 100 mW cm^{-2}, respectively.

No tumor growth inhibition was observed in Eml-RGD-treated mice (Fig. 6a and b). With the laser irradiation, the mice treated with **3** or **Eml-RGD** showed the considerable shrinkage of the tumor with dramatically higher tumor shrinkage in the latter ($p < 0.0001$, Fig. 6a and b). The body weight graph showed little toxicity of nanoemulsions **Eml-RGD** and considerable toxicity of **3** (Fig. 6c). The toxicity of **3** may be due to its low tumor-targeting effect and photodynamic damage to normal tissues (Fig. S4, ESI†). In contrast, the high therapeutic index of **Eml-RGD** was a combined result of RGDyC and EPR effect-induced high tumor targeting and high PDT effect. From tumor H&E and TUNEL staining, excess hiatus in the cell spaces and dramatic cell shrinkage indicated efficient cell destruction mediated by **3** and **Eml-RGD** with laser irradiation (Fig. 6d). Therefore, **Eml-RGD** with laser irradiation exhibited high therapeutic efficacy and low toxicity in xenograft A549 tumor mice as a result of the high tumor accumulation of **Eml-RGD**, and improved and low toxicity of PDT.

In summary, we have developed tumor-targeted multifunctional theranostics for selective detection of integrin $\alpha_v\beta_3$ over expressing cancer cells, sensitive *in vivo* tracking of the nanoemulsions, and highly efficient PDT of cancer. As versatile "add-on" modules, the amphiphilic fluorinated cryptophane-A and porphyrin self-assembled onto the surface of fluorinated nanoemulsions and turned the nanoemulsions into novel theranostics with high therapeutic index. The exquisite design of "add-on" modules not only avoided many lingering issues in regular nanomedicine, such as polydisperse polymers, heterogeneous components and complex formulation, *etc.*, but also provided the nanoparticles with multiple functions, such as tumor-targeting, complementary, quantitative and sensitive multimodal imaging (FL, ^{19}F MRI, ^{129}Xe hyper-CEST MRI), and PDT with high therapeutic index.

Furthermore, the amphiphilic "add-on" modules avoided the strong aggregation of highly hydrophobic cryptophane-A and porphyrin and, in turn, improved the imaging capability and PDT efficacy. Meanwhile, the common fluorinated dendritic structure in fluorinated cryptophane-A, porphyrin and dendron facilitated their self-assembly into stable nanoemulsions, united ^{19}F NMR signal for sensitive ^{19}F MRI, and good optical properties for fluorescence imaging and efficient PDT. Currently, drug delivery systems are becoming more and more complex, while their chance of transition to clinical application is getting slim. It would be highly beneficial to address many lingering issues in current systems, such as polydispersity, heterogeneity, and low repeatability, *etc.*, with accurate molecular design and synthesis. The development of monodisperse multifunctional "add-on" modules for versatile theranostics in this study would be a baby step in this direction.

Conflicts of interest

There are no conflicts to declare.

Notes and references

1 (a) J. Ruiz-Cabello, B. P. Barnett, P. A. Bottomley and J. W. M. Bulte, *NMR Biomed.*, 2011, **24**, 114; (b) J. C. Knight, P. G. Edwards and S. J. Paisey, *RSC Adv.*, 2011, **1**, 1415; (c) I. Tirotta, V. Dichiarante, C. Pigliacelli, G. Cavallo, G. Terraneo, F. B. Bombelli, P. Metrangolo and G. Resnati, *Chem. Rev.*, 2015, **115**, 1106.
2 (a) Q. Zeng, Q. Guo, Y. Yuan, Y. Yang, B. Zhang, L. Ren, X. Zhang, Q. Luo, M. Liu, L.-S. Bouchard and X. Zhou, *Anal. Chem.*, 2017, **89**, 2288; (b) S. Klippel, J. Döpfert, J. Jayapaul, M. Kunth, F. Rossella, M. Schnurr, C. Witte, C. Freund and L. Schröder, *Angew. Chem., Int. Ed.*, 2014, **53**, 493; (c) S. H. Klass, A. E. Truxal, T. A. Fiala, J. Kelly, D. Nguyen, J. A. Finbloom, D. E. Wemmer, A. Pines and M. B. Francis, *Angew. Chem., Int. Ed.*, 2019, **58**, 9948.
3 H. Zhang, Y. Li, S. Chen, Y. Yuan, Z.-X. Jiang and X. Zhou, *ACS Appl. Bio Mater.*, 2019, **2**, 27.
4 (a) B. M. Luby, C. D. Walsh and G. Zheng, *Angew. Chem., Int. Ed.*, 2019, **58**, 2558; (b) S. Mallidi, S. Anbil, A.-L. Bulin, G. Obaid, M. Ichikawa and T. Hasan, *Theranostics*, 2016, **6**, 2458; (c) X. Li, S. Lee and J. Yoon, *Chem. Soc. Rev.*, 2018, **47**, 1174; (d) X. Li, N. Kwon, T. Guo, Z. Liu and J. Yoon, *Angew. Chem., Int. Ed.*, 2018, **57**, 11522; (e) S. Monro, K. L. Colon, H. Yin, J. Roque, P. Konda, S. Gujar, R. P. Thummel, L. Lilge, C. C. Cameron and S. A. McFarland, *Chem. Rev.*, 2019, **119**, 797.
5 (a) X.-R. Song, S.-X. Yu, S.-H. Li, J. Li, H.-H. Yang, X. Wang, J. Cao, G. Liu and X. Chen, *Adv. Mater.*, 2015, **27**, 3285; (b) Q. Chen, X. Wang, C. Wang, L. Feng, Y. Li and Z. Liu, *ACS Nano*, 2015, **9**, 5223; (c) J. Mou, T. Lin, F. Huang, H. Chen and J. Shi, *Biomaterials*, 2016, **84**, 13; (d) S. Lu, X. Li, M. Shen, X. Shi, J. Zhang and C. Peng, *Adv. Sci.*, 2018, **5**, 1801612; (e) B. Yu, H. Wei, Q. He, F. A. Ferreira, C. J. Kutyreff, D. Ni, Z. T. Rosenkrans, L. Cheng, F. Yu, J. Engle, X. Lan and W. Cai, *Angew. Chem., Int. Ed.*, 2018, **57**, 218; (f) Y. Li, Y. Wu, J. Chen, J. Wan, C. Xiao, J. Guan, X. Song, S. Li, M. Zhang, H. Cui, T. Li, X. Yang, Z. Li and X. Yang, *Nano Lett.*, 2019, **19**, 5806.
6 (a) Z.-X. Jiang, X. Liu, E.-K. Jeong and Y. B. Yu, *Angew. Chem., Int. Ed.*, 2009, **48**, 4755; (b) S. Bo, C. Song, Y. Li, W. Yu, S. Chen, X. Zhou, Z. Yang, X. Zheng and Z.-X. Jiang, *J. Org. Chem.*, 2015, **80**, 6360; (c) S. Bo, Y. Yuan, Y. Chen, Z. Yang, S. Chen, X. Zhou and Z.-X. Jiang, *Chem. Commun.*, 2018, **54**, 3875; (d) Y. Zhang, S. Bo, T. Feng, X. Qin, Y. Wan, S. Jiang, C. Li, J. Lin, T. Wang, X. Zhou, Z.-X. Jiang and P. Huang, *Adv. Mater.*, 2019, **31**, 1806444.